Validation of a corner reflector installation at Côte d'Azur multi-technique geodetic observatory

Xavier Collilieux, Clément Courde, Bénédicte Fruneau, Mourad Aimar, Guillaume Schmidt, Isabelle Delprat, Marie-Amélie Defresne, Damien Pesce, Fabien Bergerault, Guy Wöppelmann

Version of Record: https://www.sciencedirect.com/science/article/pii/S0273117722003271
Manuscript_12176ffe17c4c6274ad5e47f4c81193a

Validation of a Corner Reflector installation at Côte d'Azur multi-technique geodetic Observatory

Xavier Collilieux[1,2], Clément Courde[3], Bénédicte Fruneau[4], Mourad Aimar[3], Guillaume Schmidt[5,2], Isabelle Delprat[5,2], Marie-Amélie Defresne[1,6] Damien Pesce[7], Fabien Bergerault[7], Guy Wöppelmann[8]

[1] Université de Paris, Institut de physique du globe de Paris, CNRS, IGN, F-75005 Paris, France.
[2] ENSG-Géomatique, IGN, F-77455 Marne-la-Vallée, France.
[3] Université Côte d'Azur, CNRS, Observatoire de la Côte d'Azur, IRD, Géoazur, 2130 route de l'Observatoire, 06460 Caussols, France.
[4] Univ Gustave Eiffel, ENSG, IGN, LASTIG, F-77454 Marne - la- Vallée, France.
[5] Enseignement Militaire Supérieur Scientifique et Technique, Ecole militaire, 75007 Paris, France.
[6] ENSTA Bretagne, 2 Rue François Verny, 29200 Brest, France.
[7] Institut national de l'information géographique et forestière, 73 avenue de Paris, 94165 Saint-Mandé, France.
[8] Laboratoire Littoral Environnement et Sociétés, UMR7266 – Univ La Rochelle and CNRS, La Rochelle, France.

Abstract

We present the procedure we followed to design an artificial corner reflector (CR) at the Calern site of Côte d'Azur Observatory (France). Although still few in number, such reflectors are an integral part of the Global Geodetic Observing System (GGOS) infrastructure. They can be used as a stable radar target in SAR images to connect local InSAR deformation maps to the global Terrestrial Reference Frame and for SAR absolute determination. During a test phase, the orientation of the CR was changed in order to be aligned toward all possible orbits of Sentinel-1A/1B satellites. On the different SAR images, the CR exhibits a high backscattering signal, and provides a Signal-to-Clutter Ratio larger than 26 dB. Since December 2018, the CR is specifically oriented toward the relative orbit 88. It is clearly detected as a PS in our InSAR analyses and as expected, the standard deviation of displacement measured on the CR is lower than on surrounding PS. A first local survey was performed to locate precisely this CR with respect to the existing geodetic instruments and annual campaigns have been carried out since then to insure its stability over time.

Key words

Corner reflector - GGOS fundamental station –PSInSAR - local survey – local tie vector – Sentinel-1A/1B

Corresponding author :
Xavier Collilieux
Tel : +33 1 64 15 31 17
E-mail : xavier.collilieux@ensg.eu

1 Introduction

Geodetic observatories play a fundamental role in the determination of the International Terrestrial Reference Frame (ITRF). They host several geodetic permanent instruments whose coordinates can be determined at the centimeter level or better. They usually include Global Navigation Satellite System (GNSS) permanent antenna/receivers, Satellite Laser Ranging (SLR) stations, Very Long Baseline Interferometry (VLBI) telescope and Doppler Orbitography Integrated by Satellite (DORIS) beacons. Calern site of the Côte d'Azur Observatory (OCA) is an example of such a multi-technique site located in the South of France. It hosts a DORIS beacon, a SLR/LLR station and two permanent GNSS stations.

In the process of determining coordinates of geodetic instruments in a unified reference frame, the relative position of the instruments at co-location sites are included as observations (Altamimi et al., 2016). Thanks to these measurements obtained from local surveys, it is possible to determine global biases between coordinates determined by individual space geodetic techniques, the so-called transformation parameters, and express them in the same reference system. A critical assumption of the ITRF combination process is that stations located at the same site do not move with respect to each other (Altamimi et al., 2016). Thus, velocities are constrained to be equal at those sites. Without such velocity constraints, it is not possible to estimate transformation parameters between GNSS, VLBI, SLR and DORIS velocity fields. This assumption of equal velocity is rarely verified with external data. Nevertheless, an example exists, at Medicina in Italy, where local motions and monument instability were reported (Sarti et al., 2013). More generally, relative motion could be either related to local ground deformation or to instrument reference point displacement (tilt of the instrument for example). The usual way to verify this assumption is to carry out repeated local surveys at regular time intervals that directly relate instrument reference points. While it is the most accurate method, this is not a widespread practice due to the cost and duration of such surveys. Alternatively Zerbini et al., (2007) investigated the use of InSAR, a remote sensing technique, to monitor ground deformation at Medicina, an ITRF co-location site. To the knowledge of the authors such experiment has never been reproduced as a systematic strategy since then although a recent computation by Poreh and Pirasteh (2020) based on X-band images at the same site can be cited. Nevertheless, the advent of the Sentinel-1 mission and the ESA open data policy, offering freely available SAR images acquired by the constellation of the 2 satellites S1-A and S1-B, with a high repeat frequency, opens the door to systematic ground deformation monitoring of ITRF co-location sites.

DInSAR technique, introduced in the 1990's (Massonet and Feigl, 1998), has been exploited to derive ground displacement fields. Different multi-temporal InSAR methods have been developed over the years to overcome the limitations of DInSAR. One of the relevant methods, PSInSAR, allows measuring ground displacement with a millimetric accuracy. It relies on identifying a series of points with coherent phase called Persistent Scatterer (PS) (Ferretti et al., 2001). It has the advantage for a set of images to provide time series of displacements on those PS with respect to one reference epoch and a reference area in the images. The displacement is given in one dimension only, along the line of sight (LOS) of the satellite. This approach can be appropriate to determine deformation maps at co-location sites, but is only effective in presence of PS, which is not guaranteed in non-urban areas of interest. One way to ensure having PS is to install active transponders (Mahapatra et al., 2014) or corner reflectors (CR) at specific known points. The second approach was adopted at OCA for its simplicity and due to the available literature on the subject.

The main motivation for the installation of a CR at the OCA observatory was thus

- to ensure getting a PS in PSInSAR analysis with high precision displacement measure in the vicinity of the OCA ITRF co-location site. PS displacement time series of natural PS at the OCA co-location sites can then be assessed with respect to this well-defined point. This point can also be observed during local ground surveys as it is the internal intersection of three plates (apex) (Garthwaite, 2017) and thus can be well controlled over time.

The following additional reasons also promoted the installation of a CR:

- to connect local InSAR deformation maps to the global Terrestrial Reference Frame, namely the ITRF. Indeed, the vertical velocity determination of the OCA geodetic observatory is likely reliable as it is measured by several techniques (Mahapatra et al., 2018).
- to provide a measurement point for absolute CR coordinate determination with SAR data as done by Gisinger et al. (2015, 2016) in a multi-technique ITRF site with TerraSAR-X data.
- to calibrate geometrically or validate the calibration of SAR sensors (Freeman, 1992)
- to evaluate the interest of installing CR close to tide gauges (TG) in France in the scope of the SONEL objectives (Wöppelmann, 2021). Indeed, GNSS permanent station vertical velocities are used to determine absolute sea level rise at TG when the instruments are co-located. For distant GNSS stations, the relative motion between the TG and the GNSS station can be determined by InSAR (Raucoules et al., 2013; Poitevin et al., 2019).

It is worth mentioning that some ITRF co-location sites are already equipped with CR, such as Wettzell, O-Higgins, Metsähovi (Gisinger et al., 2016) and Yarragadee (Thankappan et al., 2019). But it is far to be the case for all observatories. However, such reflectors are an integral part of the Global Geodetic Observing System (GGOS) infrastructure (Plag et al., 2009).

A relevant discussion on the design and installation of CR can be found in Garthwaite et al. (2015a, 2015b) and Parker et al. (2017). Our study is built on their experience by adapting the CR mount and adding survey marks to allow the deformation monitoring of the CR structure by spirit levelling over time. Besides, the CR location is here assessed on all Sentinel-1A & B orbit configurations and a validation is proposed by means of InSAR data processing.

The design of the CR is presented in section 2. Section 3 describes the analysis of SAR data prior to installation to select a relevant location for the CR and after its installation to validate it. Finally, section 4 describes the local tie survey that has been carried out to determine the CR position in the International Terrestrial Reference Frame. Such survey when repeated will allow assessing the CR sustainability and will ensure a measure of its stability. Indeed, as reported by Crosetto et al. (2016), the integrity of measurement on artificial CR has to be guaranteed over the entire monitoring period.

2 SAR Corner Reflector design

Several studies, in particular the ones of Garthwaite et al. (2015a, 2015b), and Garthwaite (2017) estimated the performance of trihedral CR of different sizes in terms of displacement error magnitude. In order to achieve a precision on the measurement of displacement smaller than 0.5 mm in C-band, as the radar instrument on board Sentinel-1 satellites, a CR with a side length (non-hypotenuse side) of 1.5 m was chosen, following the theoretical formulae in section 3.1 and the conclusions in Garthwaite et al. (2015b).

The design of our CR is shown in Fig. 1. It is adapted from Garthwaite (2015b). For cost and

technical reasons, aluminum plates are slightly smaller than 1.5x1.5m with a thickness of 8 mm. The plate inner legs are 1.440m length. Their thickness was chosen to maintain plate flatness even when subjected to high winds at the installation altitude of 1240 m above sea level. Besides, flatness and perpendicularity were measured during the manufacturing because the theoretical response of the CR in a SAR image decreases rapidly as the angle of the plates departs from 90° (Garthwaite, 2015b). The flatness default is smaller than 0.7 mm for the three plates and the perpendicularity default smaller than 0.06°.

The CR is designed to be re-oriented to various geometries of SAR satellite orbits. It can be oriented over two rotation axes. Two steel discs allow pointing the CR in azimuth. The first disc is fixed to the base. The second disc is fixed to the CR and slides on the first disc. Two threaded rods allow toggling the CR in elevation. All the CR components are powder-coated. It was fixed on a 1m x 1m concrete slab as shown in Fig. 1. The slab was built in-situ and tied-in the bedrock. It is totally hidden from the view of the SAR satellite to prevent any additional reflection.

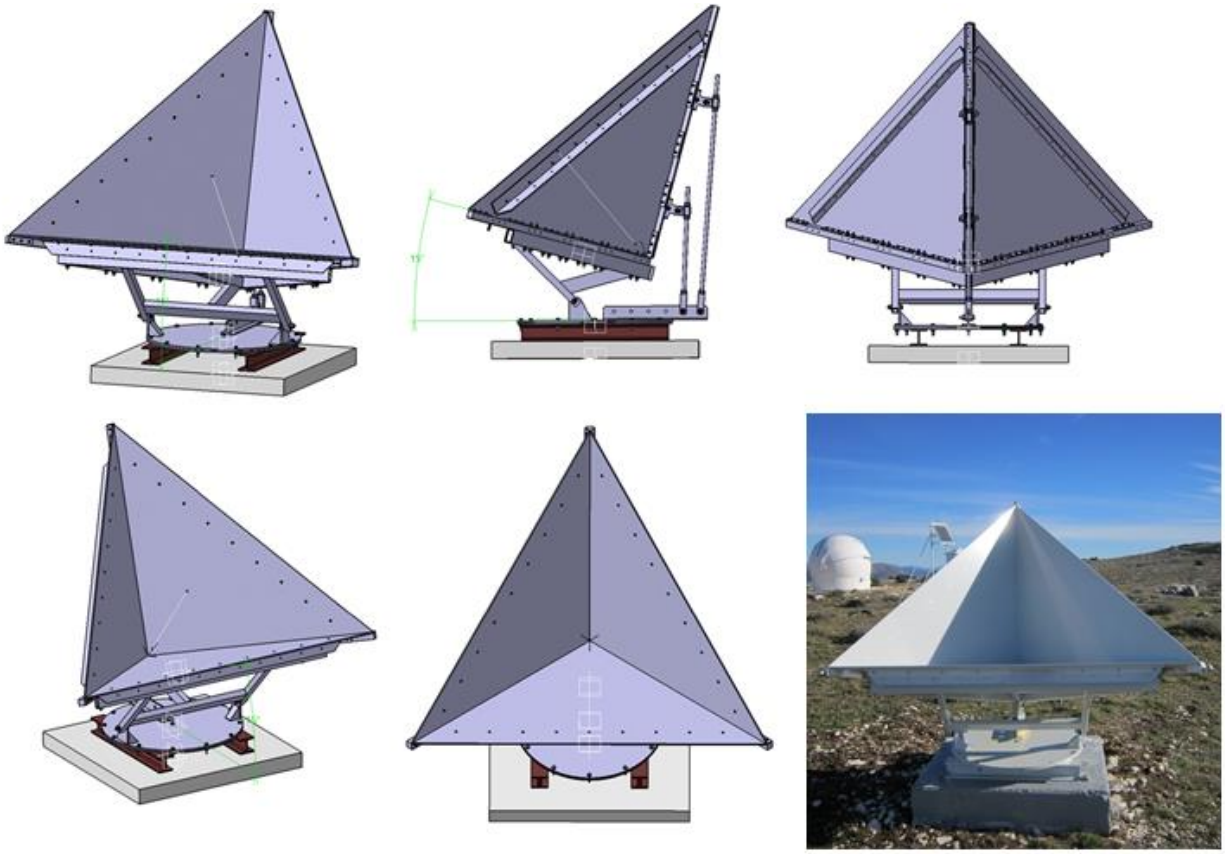

Fig. 1 Design of the CR and CR in its final location at OCA

3 Site selection and validation

3.1 Target visibility in SAR images - background

A candidate location for installing a CR should exhibit low SAR backscattered signal. In case of a distributed target, it is common to compare the observed backscattering signal to that expected from an area of one square meter. It defines the sigma-nought, a scattering coefficient which is a normalized dimensionless number, which can be computed using the calibration Look Up Table provided by ESA with Sentinel-1 images as follows:

$$\sigma^0 = \frac{A^2}{A_\sigma^2} \quad (1)$$

where A is the amplitude of a pixel in the image and A_σ is a calibration factor (Miranda and Meadows 2015). Moreover, a terrain normalization area factor correction computed from a Digital Elevation Model (DEM) can be applied to take into account the real illuminated area (Frey et al., 2013). We consider such derived sigma-nought, called terrain-corrected σ^0, to evaluate the SAR image clutter in the observatory area i.e. the intensity of backscatter response from the surrounding environment.

Installing a CR allows getting a strong response in SAR images and a high intensity at the CR location compared to the intensity of backscatter response from the surrounding environment (Parker et al., 2017). Knowing the CR design, it is possible to compute its theoretical response in a SAR image. The strength of reflection is usually expressed in terms of the geometric cross section of a conducting sphere that would give rise to the same level of reflectivity. It is called the radar cross section (*RCS*), expressed in meter squared (Garthwaite et al., 2015b). The theoretical *RCS* of a triangular trihedral CR can be computed by (Qin et al., 2013; Garthwaite et al., 2015b):

$$RCS = \frac{4\pi a^4}{3\lambda^2} \quad (2)$$

with a the size length of the corner. The theoretical *RCS* of our CR is 5854.484 m² equivalent to 37.67dB.m². It can be experimentally computed for a point target by computing the integrated energy over pixels with CR response and multiplying it by the surface of the illuminated area for one pixel (Garthwaite et al., 2017; Garthwaite personal communication, 2019). We computed the surface illuminated area S from the pixel range spacing S_R, the pixel azimuth spacing S_A and the local incidence angle θ (that considers local terrain inclination) as:

$$S = \frac{S_R S_A}{\sin\theta} \quad (3)$$

To measure the visibility of a CR, the Signal-to-Clutter Ratio (SCR) need to be computed (Garthwaite, 2017; Freeman, 1992). It is defined as:

$$SCR = \frac{\sigma_T}{<\sigma_D>} \quad (4)$$

where σ_T is the RCS of the CR in the image and $< \sigma_D >$ the ensemble average RCS of clutter near the CR. It can be computed experimentally as (Qin et al. 2013):

$$SCR = \frac{A_{corner}^2}{A_{background}^2} \quad (5)$$

Where A_{corner} is the amplitude of the CR signal in the image and $A_{background}$ an estimate of the background amplitude signal not related to the CR. The SCR should be at least 20dB and closer to 30dB for calibration targets (Garthwaite et al., 2015b; Garthwaite, 2017).

It is worth mentioning that the theoretical precision of the LOS displacement inferred from phase observations at the CR is related to SCR by (Ketelaar et al., 2004; Qin et al., 2013).

$$\sigma_{LOS} \approx \frac{\lambda}{4\pi\sqrt{2SCR}} \quad (6)$$

with λ the wavelength (5.54 cm for C-band radar on board Sentinel-1 satellites). The higher the SCR, the lower the phase variance and then the better the theoretical precision on displacement. For example a SCR value of 100 (20dB) gives a theoretical precision σ_{LOS} of 0.31 mm whereas a SCR of 50 (17db) gives a precision $\sigma_{LOS} = 0.44$ mm.

In this paper, we thus compute σ^0 and *RCS* at the CR location and then derive corresponding SCR. It is recommended to install the CR in an area with low backscatter (i.e. where the background clutter is as low as possible). This has been ensured by carrying out a preanalysis of the S-1 SAR images before the installation, as described in section 3.2.

3.2 Site description and CR location

OCA is located in South of France on the Caussols plateau close to Grasse. The map of the site is given in Fig. 2. It shows the two GNSS permanent stations on the left side (GRAS, GRAC) and the building that hosts the DORIS and SLR site in the middle (GR4B, GRSM). On the East of this main building, two towers, built in September 2015, are dedicated to atmospheric turbulence monitoring, and hereafter referred as CATS buildings.

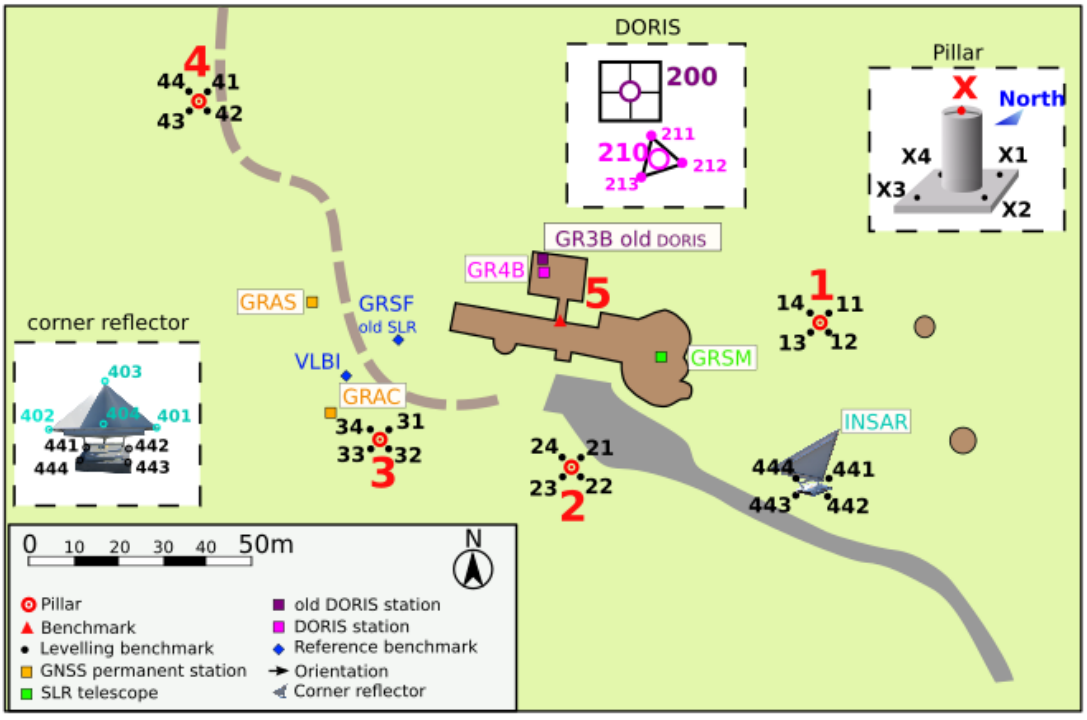

Fig. 2 Map of OCA site and its geodetic benchmarks

The CR has been designed specifically for Sentinel-1A & B satellites. Calern site is visible by these satellites from four distinct orbits, two ascending and two descending orbits, with a time revisit of 6 days. Those are usually named by the relative orbit number, which is a count of orbits from 1 to the number of orbits contained in a repeat cycle, see Table 1. The incidence angle of the satellite is either 34-35° or 43-44° depending on the orbit as indicated in Table 1.

S1A-S1B Relative Orbit number	88	161	139	66
Incidence angle (degrees)	35°	44°	34°	43°
Azimuth to the satellite (degrees)	263°	263°	96°	96°
Mean observed RCS (dBm²), see section 3.3	37.0	37.3	37.4	37.3

Table 1 Incidence angles of S-1A and S-1B satellites for different orbits at OCA, with corresponding orientation angles of the CR and mean observed RCS.

As reported by Parker et al. (2017), different constraints need to be followed to determine a relevant CR location: a clear sky visibility toward East and West, no additional multipath for GNSS stations (also for DORIS station here) and low radar backscatter signal in the area prior the installation.

A candidate location has been chosen 30 m south-west of the CATS buildings (Fig. 2). It is located 100 m from the closest GNSS stations, 70 m from the DORIS station. Fig. 3a) and Fig3c) show the map of sigma-nought before the temporary installation of the CR. It shows that σ^0 is rather small at the planned installation location. The mean terrain-corrected σ^0 computed in a 9x9 window around the CR location and averaged over the 3 images which preceded the CR installation is between -11.3 and -10.3 dB as a function of the orbit, except for orbit 139 where it reaches -8.5 dB. These values, except for orbit 139, are in the range of clutter values of flat cultivated terrain with low vegetation density recommended by Garthwaite (2017) for CR installation, which makes that location suitable for further analyses.

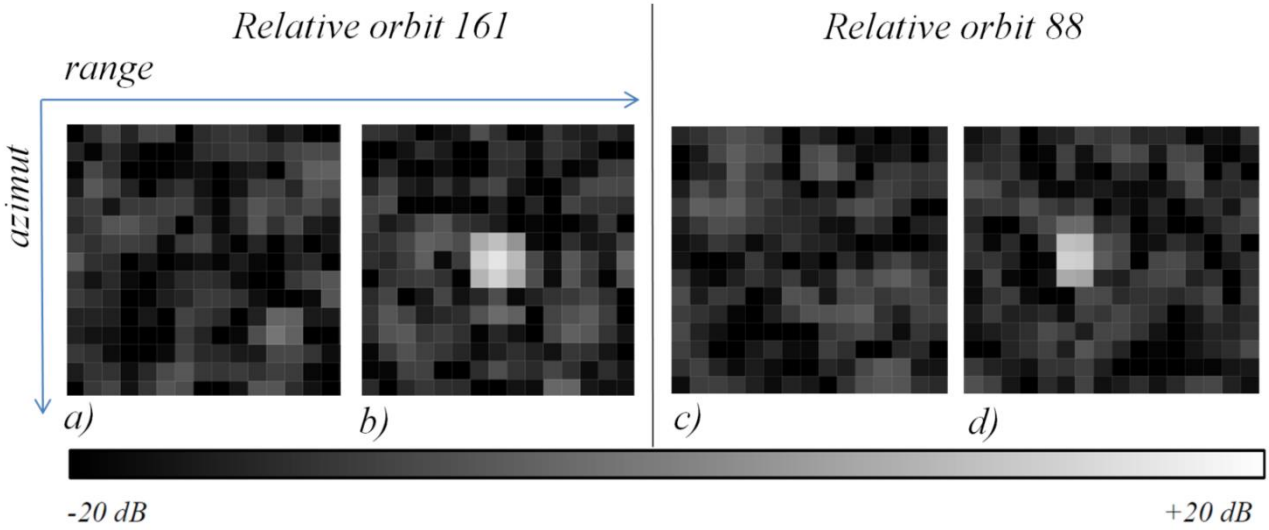

Fig. 3 left: σ^0 map in dB on the 27th of June 2018 (a) and on the 27th of July 2018, relative orbit 161(b). Right: σ^0 map in dB on the 28th of June 2018 (c) and on the 28th of July 2018, relative orbit 88 (d). Images are shown in VV polarization and radar geometry (x-axis: range; y-axis: azimuth). Images computed with SNAP software (STEP, 2019)

3.3 Site validation

A test phase was carried out to assess the candidate site location. During this phase, the CR was set up on a temporary base. It was oriented toward the satellite using a compass (precision 0.5°) and a digital level (precision 0.1°) following Garthwaite et al. (2015b, section 4.3.2) prior to each SAR image acquisition of Sentinel-1 satellites during July-August 2018. The parameters of the CR

orientation are provided in Table 1. In order to gain a maximum RCS for a trihedral CR, the CR boresight should be aligned with the SAR line of sight vector: this is obtained for an elevation of 35.26° above the baseplate of the CR (e.g. Garthwaite et al., 2015b). The azimuth and elevation of the CR boresight are given in Table 1 for each Sentinel-1 orbit.

Fig. 3b) and 3d) show typical SAR images in which the CR can clearly be identified from the four orbits. The images were processed with Gamma software (Werner et al., 2000). Three images before and three images after the installation were studied for each of the four orbits. The list of analyzed images downloaded from [dataset](Copernicus Sentinel data, 2019) is provided in the supplementary material. Following Garthwaite (2017), the SLC images were converted to sigma-nought and coregistered to a single master image (backgeocoding using the 1" SRTM Digital Terrain Model (DTM)). Their geocoding information was then updated using the same DTM to easily find the CR in the images.

The experimental RCS of the CR was determined. At first, we need identifying pixels containing CR response and pixels that will represent the backscatter intensity. The backscattered signal from the CR is spread over areas of 2x3 or 3x3 pixels as noticed in Fig. 3b. We thus define a window of 3x3 pixels centered on the pixel of the CR for computing the signal by summing the pixel values. We noted that this pixel is also the one showing the highest intensity. The backscatter intensity is computed by averaging the values of the surrounding pixels in a window of size 9x9. As done by Garthwaite (2017), the value of the integrated signal on the window 3x3 is corrected by the contribution of backscatter noise assuming it is identical in the central pixels and its surrounding.

Fig. 4a) shows the RCS determined at the CR location from the integrated CR response as described in section 3.1 from each acquisition of Sentinel-1A or 1B. There is a clear increase after the CR installation, except on the 20th of July. Indeed, during this specific day, the CR position was erroneously kept at its previous orientation in the opposite direction. This mistake was ultimately useful as it indicates that two CRs can be located in close proximity and aligned in opposite directions without interfering. The mean observed RCS are provided in Table 1– the image of the 20th of July has been excluded from the computation for the orbit 139. They agree with the theoretical value of the RCS within 0.7dBm² in average. A part of this difference could be explained by the CR alignment. Garthwaite (2017) showed that a few degrees misalignment would affect the RCS by less than about -0.2 dBm². However in addition to the alignment procedure precision, we did not consider local magnetic declination corrections during the alignment to correct our compass measurements. Yet, the magnetic declination was about 2.1° at the CR location during our test phase as computed by NOAA (2022) using the International Geomagnetic Reference Field (IGRF) model. According to the figure 4.26 of Garthwaite (2017), such an error could contribute to a bias of -0.1dBm².

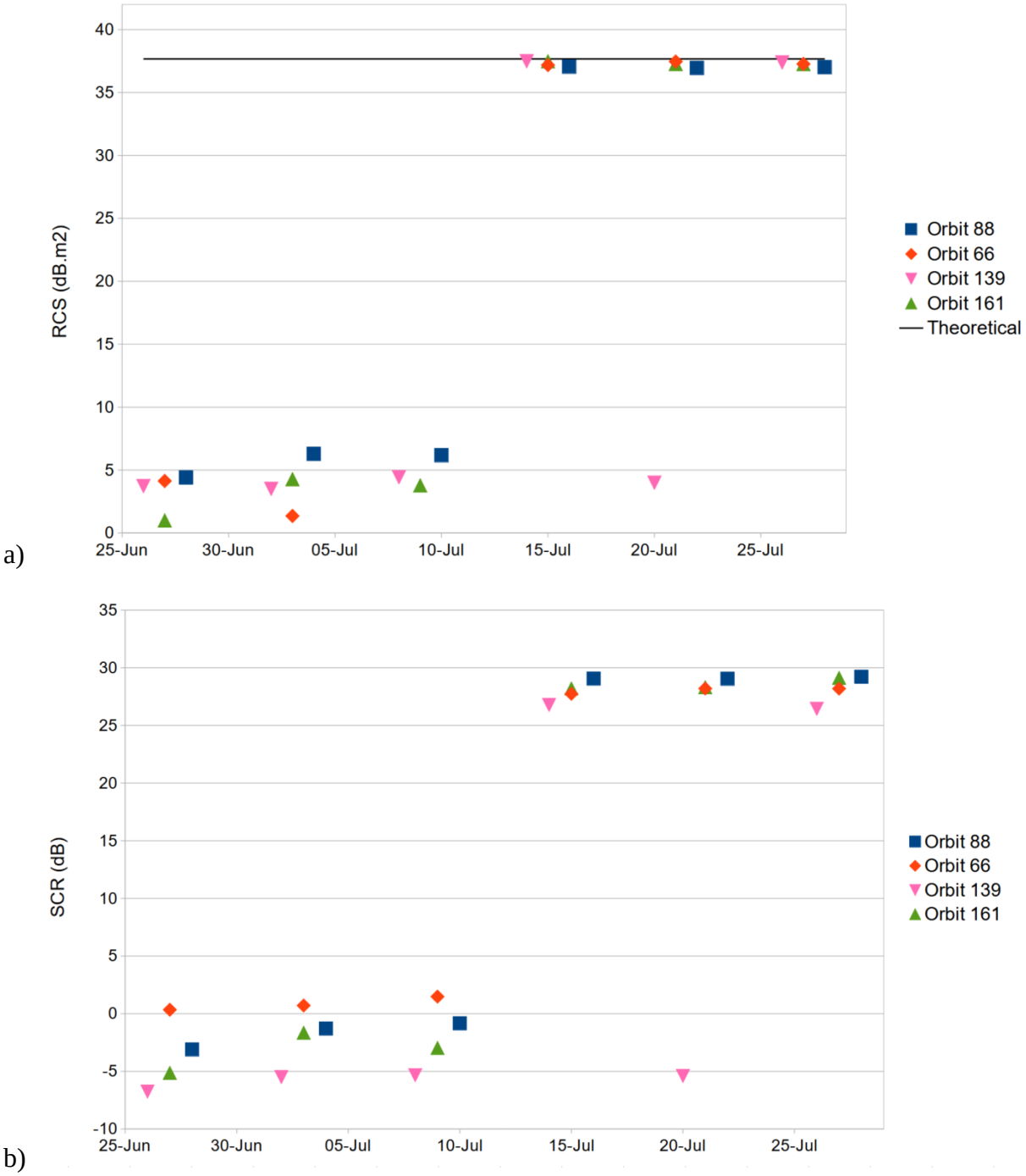

Fig. 4 a) RCS computed from SAR images and theoretical value, see section 3.1. b) SCR (dB) as a function of time.

We also followed the procedure of Garthwaite (2017) to determine the SCR experimentally. Fig. 4b) shows the resulting SCR for the test period. Its value ranges 26.4dB to 29.2dB after CR installation. This validates our choice of the location of the CR for the four relative orbits. According to Eq. (6), a precision of 0.11-0.15 mm on the measurement of displacement can be expected at the CR.

Based on these results, the decision has been taken to keep the CR oriented toward the relative orbit 88, see Table 1 for CR boresight orientation. Indeed, as for the relative orbit 139, the incidence angle is smaller which makes InSAR measurement more sensitive to the vertical component of displacement. Furthermore, the backscatter intensity is slightly smaller for orbit 88, -

10.3dB against -8.5dB for orbit 139, that is why it was retained. However, while it has not been installed mid-way between orbit 88 and 161 satellite directions, the CR is also clearly visible in orbit 161 images.

3.4 Detected PS

After the test phase described above, the CR has been settled in its definite location on a newly built concrete slab in October 2018. However it has only been anchored definitively on the 3rd of December before the survey, see section 4.

A PSInSAR analysis of the SAR images was carried out using the StaMPS software (Hooper et al., 2004; Hooper, 2012) specifically the SNAP-StaMPS integrated processing method proposed by Foumelis et al., (2018). 18 Sentinel-1 images [dataset](Copernicus Sentinel data, 2019) acquired on ascending orbits (relative orbit 88) from November 2018 to August 2019 were processed. Fig. 5a) shows the map of the detected PS from the PSInSAR analysis. They include natural points and the CR. Due to the strong response of the CR which leaks to nearby pixels, see Fig. 3, nine PS are identified. Time series of the resulting displacement at the CR are shown in Fig. 5b). The time where the CR was anchored, after the first measurement, is clearly detectable which shows the sensitivity of the InSAR measurements.

As already mentioned, the theoretical precision of the phase measurement at the CR is supposed to be a few tenths of millimeter. To verify this, we computed the standard deviations of the LOS displacement time series. The displacement at the first epoch was removed from all PS time series since the CR was not yet anchored. In addition, a common displacement series computed by the average of all PS displacement time series in a radius of 200 m around the observatory was also subtracted. This way, the mean displacement of the area which is related to the conventional choice of referencing does not affect the computed standard deviation. The colors of PS in Fig. 5a) represents the standard deviations that were computed. 292 PS are located in this radius of 200 m. The minimum, median and maximum standard deviation of the PS displacement series are respectively 0.46, 1.96 and 6.51 mm. The 5 first smallest are obtained for PS at the CR location, between 0.46 and 0.76 mm. The theoretical value of 0.14 mm is not reached here probably due to the extra noise added by removing the averaged displacement series of the reference area and residual errors. However, it can be clearly seen that the precision of the phase measurement is higher at the CR location compared to surrounding PS.

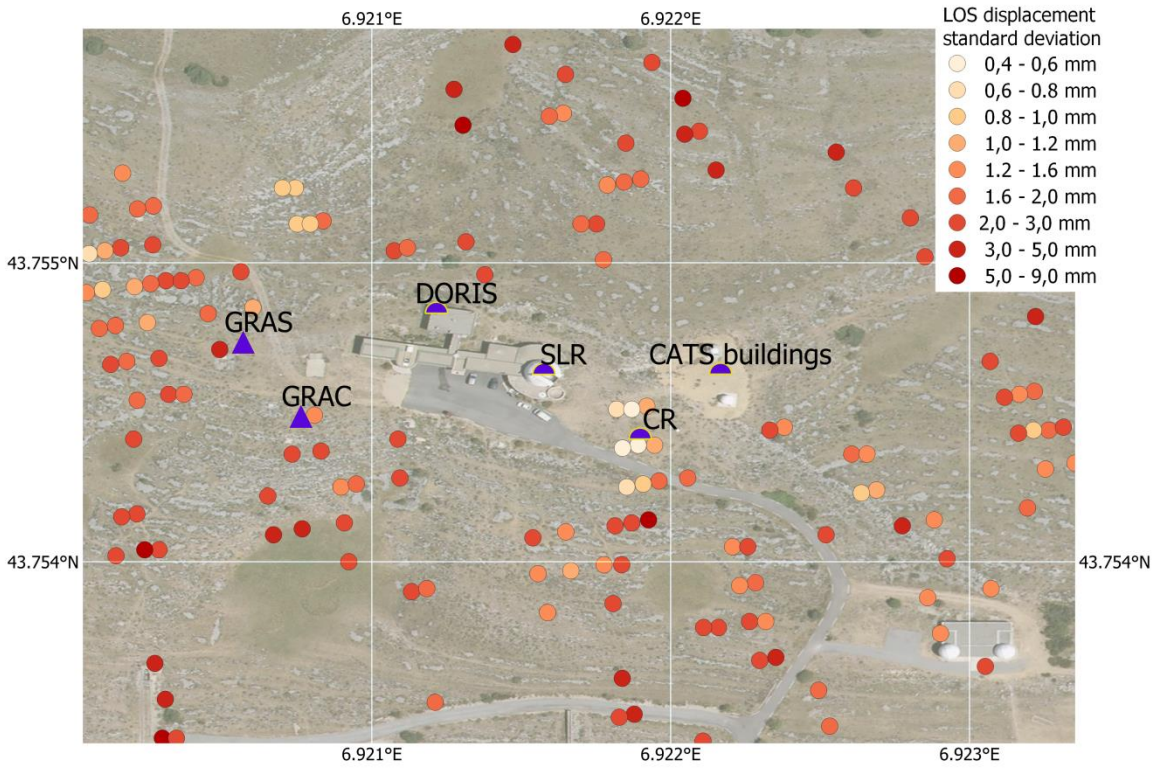

a)

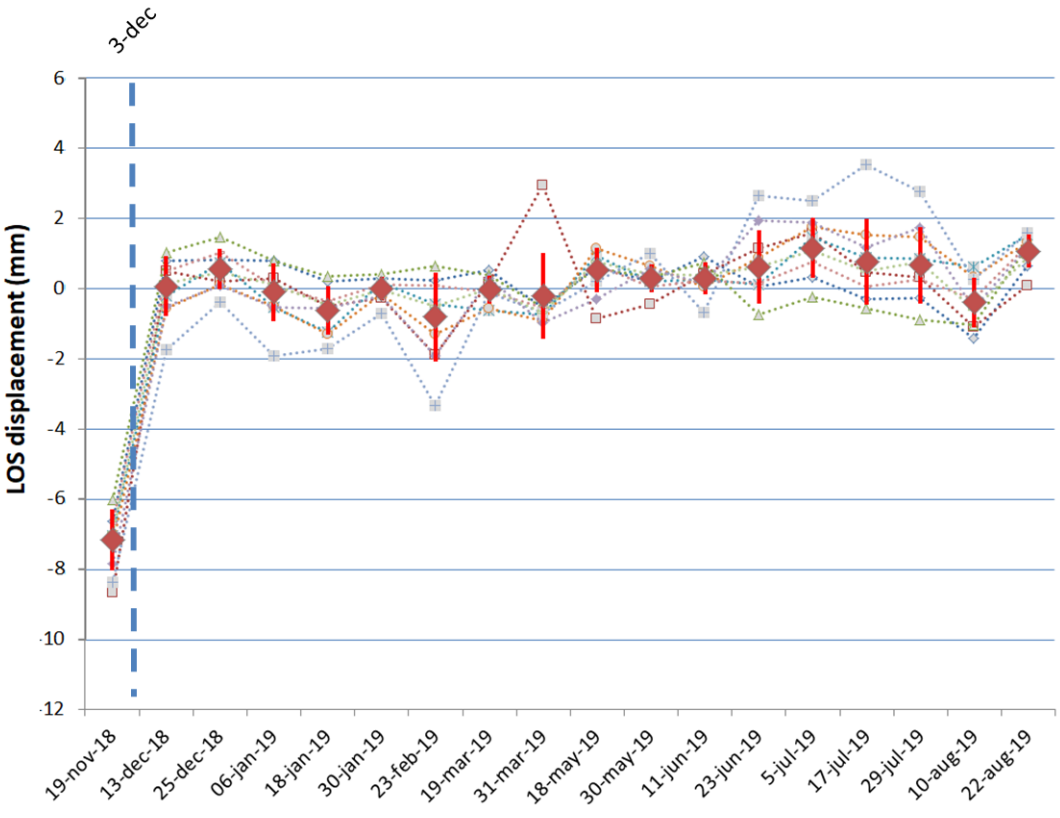

b)

Fig. 5 a) Identified PS in the vicinity of OCA after CR installation. Standard deviations of the LOS displacement time series are shown in mm after the removal of the reference area displacement time series. b) LOS displacement time series at the 9 pixels of the CR. The mean displacement and its standard deviation are plotted as red diamonds with red error bars

3.5 Impact on GNSS permanent station and DORIS measurements

The reason for installing the CR away from the GNSS permanent stations is to avoid multi-path. Indeed, GNSS incoming signals from satellites reflected by the CR might be observed by close GNSS stations and thus could affect the quality of their raw data. In order to assess possible multi-path effects, instead of processing GNSS data as proposed by Parker et al. (2017), we analyzed the multi-path linear combinations computed for the GNSS pseudo-range and phase raw data of the two permanent stations. Indeed, time variations in these combinations highlight changes in multipath effects (Estey and Meertens, 1999). Fig. 6a shows the combination for GPS L1 and Glonass G1 frequencies at station GRAC which is the closest to the permanently installed CR. It has been provided by the European Permanent Network (EPN) central bureau (Bruyninx et al., 2012, EPN 2019) and based on results obtained with the software G-Nut/Anubis version 2.2.1 (Vaclavovic and Dousa, 2016). It is worth reminding that the test phase started on the day 194 of 2018 (13st of July). The CR was moved on the 5th of September and installed in its final location on the day 274 (1st of October). No substantial change can be observed in Fig. 6 around these dates proving that the CR did not degrade GNSS raw observations although both devices are inter-visible and distant by 100 m. The same conclusion holds for GRAS station and other GNSS frequencies.

No significant impact on the DORIS station GR4B has been noted either. Fig. 6) shows the DORIS station residuals RMS computed from a Precise Orbit Determination analysis during the years 2018-2019. The background dynamic and measurement models employed in this analysis are consistent with the IERS 2010 Conventions (Petit and Luzum 2010) and CNES' release "F" of Medium Orbit Ephemerides (MOE) standard; see Picot et al. (2018) for details. RMS fluctuations are visible but do not seem to correlate with the installation of the CR. This was expected since the DORIS station is located on top of the roof and at a distance of 70 m.

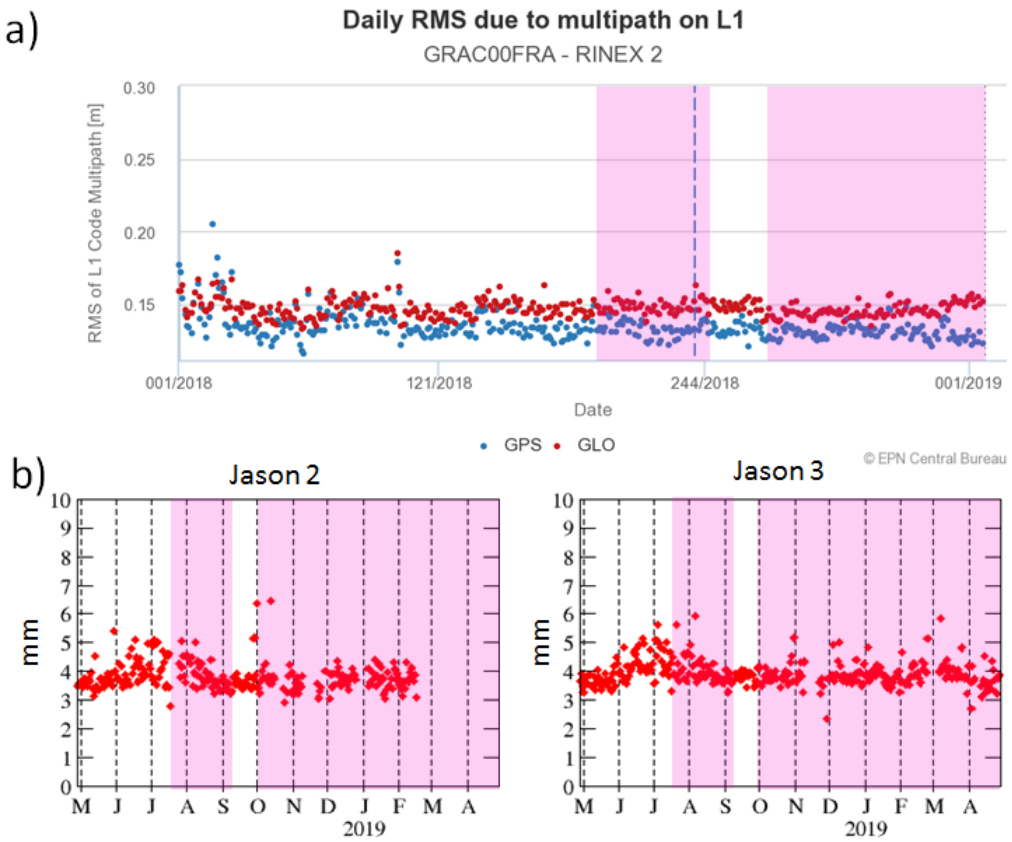

Fig. 6 a) Multipath linear combination at station GRAC at L1 frequency. Source: (EPN, 2019). b) DORIS GR4B station residual RMS per day for Jason 2 and Jason 3 satellites. Source: (IDS, 2019). For both images, periods with CR

deployed are plotted in pink.

4 Local tie survey

The Calern co-location site of the OCA was surveyed by IGN in 1995, 1999, 2003 and 2013. A new survey was performed in December 2018 in order to determine the position of the CR with respect to other space geodetic instruments of the site. A survey including all the available space geodetic instruments has not been carried out; only the tridimensional vectors between permanent survey pillars (Fig. 2) and the new CR were determined at this time.

Before the survey, leveling benchmarks have been anchored at each corner of the concrete base of the CR, see benchmarks 441-444 on Fig. 2. Thus any tilt of the monument can be detected by leveling in the future. To further monitor the deformation of the CR itself, leveling balls have been fixed to each of its corners.

The benchmarks, the pillar reference points and the intersection of the three corner plates of the CR were leveled and determined by topometry following the recommendations of Poyard et al. (2017). The observation adjustment was performed using IGN homemade software COMP3D. The coordinates were obtained with standard deviations (1 sigma) that range 2 to 5 mm in both horizontal components and less than 1 mm in vertical. At first, the coordinates of common points with the previous survey (Pesce et al., 2013) were compared. The differences are negligible in vertical and reach up to 5 mm in horizontal with a typical value of 2 mm, which is consistent with the standard deviations. The coordinates of the apex of the CR have been computed in ITRF2008 (Altamimi et al., 2011) at epoch 2013.56 in order to be consistent with the local tie product computed by Pesce et al. (2013). They are provided in Table 2 with the baseline vector from the GRAS GNSS permanent network to the CR. The latter can be added to the GRAS station coordinates at the any epoch and in any other ITRF frame to update the coordinates of the CR. This approach was followed to compute the IGb14 coordinates of the CR at epoch 2020.0 in Table 2.

	X (m)	Y(m)	Z(m)
CR position (ITRF2008@2013.56)	4581703.975	556222.822	4389335.185
CR position (IGb14@2020.00)	4581703.877	556222.940	4389335.253
	ΔX (m)	ΔY(m)	ΔZ(m)
Vector GRAS to CR	13.184	107.821	-25.713

Table 2 Position of the apex of the CR in ITRF2008 at epoch 2013.56. The baseline between GRAS and the CR is also provided.

Control leveling measurements were carried out in March 2019 and March 2021 by ENSG-géomatique engineer students. The heights of some benchmarks and some CR leveling balls exhibited changes up to 2.0 mm with respect to a reference marker. Due to their variability, these variations are suspected to be caused by measurement errors. However, it is reasonable to conclude that the CR deformation is lower than 2 mm.

5 Conclusion

A CR has been installed permanently at OCA in December 2018 following a test phase in

summer 2018. It is currently oriented toward the Sentinel 1A-1B relative orbit 88. The coordinates of the apex of the CR three intersecting plates in this orientation were determined by means of a local survey with a horizontal precision of 5 mm and a vertical precision of 1 mm in ITRF2008. The orientation of the CR has been fixed in order to provide a PS for long term analyses but it could be temporarily oriented for specific scientific experiments on request. The CR is surveyed yearly in order to monitor any relative motion, tilt of the slab or deformation of its structure.

The procedure proposed by Parker et al. (2017) was followed in order to validate this installation. As four Sentinel-1 orbit configurations were available, all of them were investigated. No GNSS multipath signal was detected at the closest GNSS stations which are separated by 100 m according to the GPS multipath linear combination analysis. The SCR measured in Sentinel-1 images is larger than 26dB, which should provide a theoretical phase measurement precision smaller than 0.15 mm. By processing 18 Sentinel-1 SAR images, we have been able to detect the CR as a PS and identify the time at which the CR has been anchored to its base. The precision of the deformation measurement has been evaluated with real data to be of the order of 0.5 mm at the CR which is higher compared to surrounding PS, 2.0 mm in average. The proposed approach by Parker et al. (2017) is reproducible and can therefore be recommended for the installation of new corner reflectors at fundamental GGOS sites.

Thanks to this CR, OCA observatory now benefits from a stable PS. It will be surveyed regularly to monitor its stability and integrity with time. As soon as more Sentinel-1 data are accumulated, this PS will be useful to accurately tie InSAR derived ground deformation maps to the geodetic reference system/datum. In addition, if properly oriented as a function of the satellite mission used, its absolute coordinate could be computed by means of absolute SAR methods, thus providing a new geodetic technique at OCA.

6 Acknowledgment

This study contributes to the IdEx Université de Paris ANR-18-IDEX-0001. It was supported by the Programme National GRAM of CNRS/INSU with INP and IN2P3 co-funded by CNES but also by BQR-OCA. The survey work would not have been possible without Pierre Cumerlato. We thank the S2M of OCA for their work on the design, the manufacture and the implementation. We are also grateful to Aelaig Cournez and Hugo Bontempi, both students at ENSG, who studied the computation of the SCR of the CR as well as Hugo Lecomte for his advises. The ENSG-géomatique students who carried out yearly local tie surveys at OCA were supervised by Jacques Beilin. We thank them through him. We also particularly thank Sébastien Giordano for providing his lecture notes, useful documentations and his support as well as Daniel Raucoules and Marc Poupée for their help at the beginning of the project. Finally, we thank Matthiew Garthwaithe who reviewed a first version of this manuscript for his insightful comments and suggestions as well as the three anonymous reviewers and the editor Pascal Willis.

7 References

Altamimi Z, Rebischung P, Métivier L, Collilieux X. ITRF2014: A new release of the International Terrestrial Reference Frame modeling nonlinear station motions, J Geophys Res 2016, 121(B8), 6109-6131, doi:10.1002/2016JB013098.

Altamimi Z, Collilieux X, Métivier L, ITRF2008: an improved solution of the International Terrestrial Reference Frame, Journal of Geodesy 2011, 85, 8, 457-473, doi:10.1007/s00190-011-0444-4.

Bruyninx C, Habrich H, Söhne W, Kenyeres A, Stangl G, Völksen C, Enhancement of the EUREF Permanent Network Services and Products, "Geodesy for Planet Earth", IAG Symposia Series, 2012, 136, 27-35, doi:10.1007/978-3-642-20338-1_4.

[dataset] Copernicus Sentinel data, 2019, Sentinel 1A/1B Level-1 Interferometric Wide Swath SLC images, available at Copernicus Services Data Hub, https://scihub.copernicus.eu/dhus/#/home

Crosetto M, Monserrat O, Cuevas-González M, Devanthéry N, Crippa B. Persistent Scatterer Interferometry: A review, ISPRS J Photogrammetry Remote Sens, 2016, 115, 78 – 89, doi:10.1016/j.isprsjprs.2015.10.011.

EPN, EUREF Permanent GNSS Network, Daily Tracking Performances, 2019 (Accessed February, 2019, at http://www.epncb.oma.be/_networkdata/data_quality/index.php?station=GRAC00FRA)

Estey L, Meertens CM. TEQC: The Multi-Purpose Toolkit for GPS/GLONASS Data, GPS Solut 1999, 2, 1, 42-49.

Ferretti A, Prati C, Rocca F, Permanent scatterers in SAR interferometry, IEEE Transactions on Geoscience and Remote Sensing 2001, 39, 1, 8-20.

Foumelis M, Delgado JM, Desnos YL, Engdahl M, Fernandez D, Veci JLL, Wong C. ESA SNAP - StaMPS integrated processing for sentinel-1 persistent scatterer interferometry, IEEE Int. Geosci Remote Sens Symposium. IGARSS 2018, 1, 3.2.

Freeman A. SAR calibration: An overview, IEEE Transactions on Geoscience and Remote Sensing 1992, 30, 6, 1107-1121, doi:10.1109/36.193786.

Frey O., M. Santoro, C. L. Werner and U. Wegmuller, DEM-Based SAR Pixel-Area Estimation for Enhanced Geocoding Refinement and Radiometric Normalization, in IEEE Geoscience and Remote Sensing Letters 2013, 10, no. 1, pp. 48-52, Jan., doi: 10.1109/LGRS.2012.2192093.

Garthwaite MC. On the design of Radar Corner Reflectors for Deformation Monitoring in Multi-Frequency InSAR, Remote Sensing 2017, 9, 648, doi:10.3390/rs9070648.

Garthwaite MC, Hazelwood M, Nancarrow S, Hislop A, Dawson JH. A regional geodetic network to monitor ground surface response to resource extraction in the northern Surat Basin, Queensland, Aust J Earth Sci 2015a, 62, 4, doi:10.1080/08120099.2015.1040073.

Garthwaite MC, Nancarrow S, Hislop A, Thankappan M, Dawson JH, Lawrie S. The Design of Radar Corner Reflectors for the Australian Geophysical Observing System. A single design suitable

for InSAR deformation monitoring and SAR calibration at multiple microwave frequency bands, Geoscience Australia record 2015/03, 2015b.

Gisinger C, Balss U, Pail R, Zhu XX, Montazeri S, Gernhardt S, Eineder M. Precise Three-Dimensional Stereo Localization of Corner Reflectors and Persistent Scatterers With TerraSAR-X, IEEE Transactions geoscience remote sens 2015, 53, 4, 1782-1802, doi:10.1109/TGRS.2014.2348859.

Gisinger C, Willberg M, Balss U, Klügel T, Mähler S, Pail R, Eineder M. Differential geodetic stereo SAR with TerraSAR-X by exploiting small multi-directional radar reflectors, J Geodesy 2016, 91, 53-67, doi:10.1007/s00190-016-0937-2.

Hooper A, Bekaert D, Spaans K, Arikan M. Recent advances in SAR interferometry time series analysis for measuring crustal deformation, Tectonophysics 2012, 514-517, 1-13, doi:10.1016/j.tecto.2011.10.013.

Hooper A J, Zebker H, Segall P, Kampes P, A new method for measuring deformation on volcanoes and other natural terrains using InSAR persistent scatterers, Geophys Res Lett 2004, 31, L23611, doi:10.1029/2004GL021737.

IDS, International DORIS Service web site, 2019 (Accessed July 13, 2019, at https://ids-doris.org/system/36-moe/62-moe-data.html?sta=GR4B)

Ketelaar G, Marinkovic P, Hanssen R, Validation of Point Scatterer Phase Statistics in Multi-Pass INSAR, Porc. Of the 2004 Envisat &ERS Symposium 2005, ESA-SP Vol. 572.

Mahapatra P, Samiei-Esfahany S, van der Marel H, Hanssen R, On the Use of Transponders as Coherent Radar Targets for SAR Interferometry, IEEE Transactions on Geoscience and Remote Sensing 2014, 52, 3, 1869-1878, doi: 10.1109/TGRS.2013.2255881.

Mahapatra P, van der Marel H, van Leijen F, Samiei Esfahany S, Klees R, Hanssen R, InSAR datum connection using GNSS-augmented radar transponders, J Geodesy 2018, 92, 1, 21-32, doi: 10.1007/s00190-017-1041-y.

Massonet D, Feigl K, Radar interferometry and its application to changes in the Earth's surface, review geophys 1998, 36, 4, 441-500, doi:10.1029/97RG03139.

Miranda N, Meadows PJ Radiometric Calibration of S- 1 Level-1 Products Generated by the S-1 IPF, ESA, 2015, 13p.

NOAA, 2022, NCEI Geomagnetic Calculators, National Centers for Environmental Information (Accessed April, 2022, at https://www.ngdc.noaa.gov/geomag/calculators/magcalc.shtml#declination)

Parker AL, Featherstone WE, Penna NT, Filmer MS, Garthwaite MC. Practical Considerations before Installing Ground-Based Geodetic Infrastructure for Integrated InSAR and cGNSS Monitoring of Vertical Land Motion. Sensors 2017, 17, 8, 1753. doi:10.3390/s17081753.

Petit G. and Luzum B. (eds.), IERS Conventions, IERS Technical Note 36, 2010, Frankfurt am Main: Verlag des Bundesamts für Kartographie und Geodäsie, 179 pp., ISBN 3-89888-989-6

Picot N, Marechal C, Couhert A, Desai S, Scharroo R, Egido A, Jason-3 products handbook, 2018, SALP-MU-M-OP-16118-CN1(5):28–3

Poitevin C, Wöppelmann G, Raucoules D, Le Cozannet G, Marcos M, Testut L. Vertical land motion and relative sea level changes along the coastline of Brest (France) from combined space-borne geodetic methods. Remote Sensing Env, 2019, 222, 275-285, doi: 10.1016/j.rse.2018.12.035.

Poreh, D., Pirasteh, S. (2020). InSAR observations and analysis of the Medicina Geodetic Observatory and CosmoSkyMed images. Natural Hazards, 103(3), 3145-3161

Qin Y, Perissin D, Lei L. The Design and Experiments on Corner Reflectors for Urban Ground Deformation Monitoring in Hong Kong, Int J Antennas Propag, 2013, 2013, Article ID 191685, 8 pages, doi:10.1155/2013/191685.

Pesce D, ITRF Co-location Survey Observatoire de la Côte d'Azur Plateau de Calern (Grasse), France, version 1, IGN technical report 28476, 2013. (Accessed July 17, 2019, at http://itrf.ign.fr/doc_ITRF/CR279_V1_PESCE_ITRFcolocationSurveyCalern.pdf).

Plag H. P., Rothacher M., Pearlman M., Neilan R., Ma C., The global geodetic observing system. Advances in Geosciences, 2009, 13, pp. 105-127.

Poyard J-C, Collilieux X, Muller J-M, Garayt B, Saunier J. IERS technical note 39 - IGN best practice for surveying instrument reference points at ITRF co-location sites, Frankfurt am Main: Verlag des Bundesamts für Kartographie und Geodäsie (ISBN 978-3-86482-129-5), 2017.

Raucoules D, Le Cozannet G, Wöppelmann G, de Michele M, Daag A, Marcos M. High nonlinear urban ground motion in Manila (Philippines) from 1993 to 2010 observed by DInSAR: implications for sea-level measurement, Remote Sensing Env, 2013, 139, 386-397. doi:10.1016/j.rse.2013.08.021.

Sarti P, Abbondanza C, Legrand J, Bruyninx C, Vittuari L, Ray J. Intrasite motions and monument instabilities at Medicina ITRF co-location site, Geophys J Int, 2013, 192, 3, 1042-1051, doi:10.1093/gji/ggs092.

STEP Science Toolbox Exploitation Platform: SNAP, 2019 (Accessed July 26, 2019, at http://step.esa.int/main/toolboxes/snap).

Thankappan, M., Fuhrmann, T., Batchelor, J., Gisinger, C., Garthwaite, M., & Miranda, N. Updates to the Australian corner reflector array coordinates and resulting improvements in absolute location error of SAR products, Proceedings CEOS CAL / VAL Workshop, 2019, https://calvalportal.ceos.org/sarcv

Vaclavovic P, Dousa J. G-Nut/Anubis - open-source tool for multi-GNSS data monitoring, In: IAG Symposia Series, Springer, 2016, 143, 775-782, doi:10.1007/1345_2015_157.

Werner C, Wegmüller U, Strozzi T and Wiesmann A (2000), GAMMA SAR and interferometric processing software, In European Space Agency, (Special Publication) ESA SP. 461, 211-219.

Wöppelmann G., Gravelle M., Testut L. SONEL sea-level observing infrastructure: French contribution to the IUGG Centennial in 2019, and beyond, Collection du Bureau des Longitudes Ed. C. Boucher, 2021, 1, 43-53.

Zerbini S, Richter B, Rocca F, van Dam T, Matonti F. A Combination of Space and Terrestrial Geodetic Techniques to Monitor Land Subsidence: Case Study, the Southeastern Po Plain, Italy. J Geophys Res, 2007, 112, 5401, doi: 10.1029/2006JB004338.

8 Figure captions

Fig. 1 Design of the CR and CR in its final location at OCA

Fig. 2 Map of OCA site and its geodetic benchmarks

Fig. 3 left: σ^0 map in dB on the 27th of June 2018 (a) and on the 27th of July 2018, relative orbit 161(b). Right: σ^0 map in dB on the 28th of June 2018 (c) and on the 28th of July 2018, relative orbit 88 (d). Images are shown in VV polarization and radar geometry (x-axis: range; y-axis: azimuth). Computed with SNAP software (STEP, 2019)

Fig. 4 a) RCS computed from SAR images and theoretical value, see section 3.1. b) SCR (dB) as a function of time.

Fig. 5 a) Identified PS in the vicinity of OCA after CR installation. Standard deviations of the LOS displacement time series are shown in mm after the removal of the reference area displacement time series. b) LOS displacement time series at the 9 pixels of the CR. The mean displacement and its standard deviation are plotted as red diamonds with red error bars

Fig. 6 a) Multipath linear combination at station GRAC at L1 frequency. Source: (EPN, 2019). b) DORIS GR4B station residual RMS per day for Jason 2 and Jason 3 satellites. Source: (IDS, 2019). For both images, periods with CR deployed are plotted in pink.